Nanoscale Advances

ROYAL SOCIETY OF CHEMISTRY

PAPER

View Article Online
View Journal | View Issue

Cite this: *Nanoscale Adv.*, 2025, **7**, 1287

Smart drug delivery: a DFT study of C_{24} fullerene and doped analogs for pyrazinamide†

Azam Moumivand,[a] Fereshteh Naderi, *[a] Omid Moradi [a] and Batoul Makiabadi[b]

The potential applicability of the C_{24} nanocage and its boron nitride-doped analogs ($C_{18}B_3N_3$ and $C_{12}B_6N_6$) as pyrazinamide (PA) carriers was investigated using density functional theory. Geometry optimization and energy calculations were performed using the B3LYP functional and 6-31G(d) basis set. Besides, dispersion-corrected interaction energies were calculated at CAM (Coulomb attenuated method)-B3LYP/6-31G(d,p) and M06-2X/6-31G(d,p) levels of theory. The adsorption energy (E_{ads}), enthalpy (ΔH), and Gibbs free energy (ΔG) values for C_{24}-PA, $C_{18}B_3N_3$-PA, and $C_{12}B_6N_6$-PA structures were calculated. The molecular descriptors such as electrophilicity (ω), chemical potential (μ), chemical hardness (η) and chemical softness (S) of compounds were investigated. Natural bond orbital (NBO) analysis confirms the charge transfer from the drug molecule to nanocarriers upon adsorption. Based on the quantum theory of atoms in molecules (QTAIM), the nature of interactions in the complexes was determined. These findings suggest that C_{24} and its doped analogs are promising candidates for smart drug delivery systems and PA sensing applications, offering significant potential for advancements in targeted tuberculosis treatment.

Received 9th July 2024
Accepted 6th December 2024

DOI: 10.1039/d4na00560k

rsc.li/nanoscale-advances

Introduction

Tuberculosis (TB) is a prevalent and often fatal infectious disease caused by various species of mycobacteria, particularly *Mycobacterium tuberculosis*.[1] TB remains one of the most significant infectious diseases of our time, capable of affecting all organs of the body, especially the lungs. Despite widespread optimism in the 1980s that TB would be controlled by the turn of the century, the World Health Organization (WHO) declared it a global emergency in 1993.[2,3] According to WHO reports, approximately 10 million people were diagnosed with TB in 2017, with the number increasing to about 6.4 million in 2019. Annually, around 1.3 million patients succumb to TB.[4] The treatment of TB has become increasingly challenging due to the emergence of drug-resistant strains of *Mycobacterium tuberculosis*. In 2012, there were about 45 000 cases of multidrug-resistant TB (MDR-TB), resulting in an estimated 170 000 deaths. The situation is exacerbated when these strains develop resistance to multiple drugs, undermining the significant advances made in TB control over the past century.[5] Currently, more than 8 million people worldwide contract TB each year, and approximately one-third of the global population harbors the bacterium asymptomatically. Despite significant efforts to control TB, the emergence of drug resistance remains a critical concern, underscoring the need for rapid and accurate diagnosis to facilitate timely and effective treatment.

One of the four first-line anti-tuberculosis drugs is pyrazinamide (PA), which, in addition to shortening the treatment period from nine to six months, eradicates the organism by destroying the active and inactive forms of bacillus tuberculosis in the acidic environment inside the macrophages.[6] Like other drugs, PA has important side effects, such as fever, anorexia, liver enlargement, jaundice, and liver failure. Targeted drug delivery is a new way to reduce problems caused by direct drug use and drug resistance.[7–9] Considering the common challenges of using drugs such as PA, the controlled release of the drug has attracted the attention of researchers. Targeted drug delivery and controlled release has advantages such as the possibility of drug delivery in nanometer dimensions, the ability to maintain the drug concentration in a relatively constant amount for a certain time, the ability to adjust the drug release rate depending on the place of drug delivery, and the ability to transfer several drug substances to a specific tissue or organ.[10,11] Nowadays, drug delivery based on nanocarriers is at the center of attention of many companies acting in the pharmaceutical industry since nanomaterials have special properties and potential applications that make them superior to the traditional drug delivery vectors. The use of nanocarriers in medical science helps to increase the availability of the drug at the site of disease, and reduces the dose frequency and adverse side effects.[12–15] As new drugs are developed, significant efforts have been directed toward exploring innovative delivery routes.

[a]*Department of Chemistry, Shahr-e-Qods Branch, Islamic Azad University, Tehran, Iran. E-mail: fnaderi1@gmail.com; Neginmmm64@gmail.com; moradi.omid@gmail.com; Web: https://scholar.google.com/citations?user=pdCrLOYAAAAJ&hl=en*

[b]*Department of Chemical Engineering, Sirjan University of Technology, Sirjan, Iran. E-mail: bmakiabadi@yahoo.com; Web: https://scholar.google.com/citations?user=N6z-rHsAAAAJ&hl=en*

† Electronic supplementary information (ESI) available. See DOI: https://doi.org/10.1039/d4na00560k

Targeted delivery systems represent a promising solution to overcome the limitations of conventional methods. To realize this potential, a wide range of nanoparticles have been proposed and extensively studied.[16–20] These nanoparticles must interact well with biological environments and pass through the cell membrane to deliver therapeutic molecules. Fullerenes (C_{60}) are one of the pioneering classes of carbon-based nanoparticles, which have been widely studied for targeted drug delivery applications.[21] Fullerenes have a unique structure and have suitable properties for interaction with drugs. Although fullerene toxicity is somewhat of a concern, several water-soluble fullerene derivatives have shown acceptable cytotoxicity for drug delivery applications.[22] Recently, new fullerene-like compounds and hexagonal boron nitrides have been developed, and their potential applications as advanced delivery systems have been investigated.[23–27] Studies provide a detailed drug interaction mechanism with boron nitride fullerenes (BNF) and reveal that the BNF can be a smart drug delivery vehicle for the drugs.[23,28–30] In this study, the interaction of the pyrazinamide drug with C_{24}, $C_{18}B_3N_3$, and $C_{12}B_6N_6$ nanocages was investigated using density functional theory (DFT) calculations. To achieve this, we employed a range of analytical tools, including adsorption energy (E_{ads}), thermochemical parameters (ΔH and ΔG), frontier molecular orbitals, ionization energy, electrophilicity, chemical hardness, softness, electronegativity, natural bond orbitals (NBO), and atoms in molecules (AIM), as well as NMR, IR, and UV-Vis spectroscopy. These comprehensive analyses provide a detailed understanding of the interaction mechanisms and potential applications of these nanocages in drug delivery and sensing systems.

Computational details

All of the calculations were performed using the Gaussian 09 package.[31] In the first stage, geometry optimization and energy calculations were carried out using the B3LYP[32,33] functional and 6-31G(d)[34] basis set. Besides, dispersion-corrected adsorption energies employing CAM-B3LYP[35] and M06-2X[36] functionals with the 6-31G(d,p)[34] basis set were calculated. The counterpoise procedure (CP)[37] was used to correct for basis set superposition error (BSSE) in the calculation of the adsorption energies. To obtain the thermal and Gibbs free energies and ensure that the optimized structures are true local minima on the potential energy surface (not saddle points or transition states), the vibrational frequency calculations were performed at all computational levels. All reported structures were identified as true minima on the PES. The adsorption energy (E_{ads}) of the obtained structures of the interaction between pristine and doped C_{24} with PA at $T = 298$ K and $P = 1$ atm is given by the following equation:

$$E_{ads} = E_{complex} - (E_{nanocage} + E_{PA}) \quad (1)$$

Natural bond orbital analysis provides a chemical viewpoint of van der Waals interactions using a donor–acceptor type interpretation of molecular orbitals.[38] Therefore, we used NBO analyses to calculate the charge distribution over the atoms of interacting species and to estimate the stabilization energies ($E^{(2)}$) of bond–antibond interactions. The energy difference between the highest occupied (HOMO) and the lowest unoccupied molecular orbital (LUMO), known as E_g, for a system is given as:

$$E_g = E_{LUMO} - E_{HOMO} \quad (2)$$

The electronic sensitivity of the pristine and doped C_{24} nanocage toward PA is calculated as follows:

$$\Delta E_g = \frac{(E_g\ \text{complex} - E_g\text{nanocage})}{E_g\text{nanocage}} \times 100 \quad (3)$$

Quantum molecular descriptors (also known as the conceptual density functional theory (CDFT) parameters), including the electronegativity (χ), global hardness (η), electrophilicity index (ω), ionization potential (I), electron affinity (A), and electronic chemical potential (μ), were calculated with the help of HOMO and LUMO values. The electrophilicity index (ω) measures the stability of a compound in the presence of an additional electronic charge from the environment. In a charge transfer process, higher values of ω indicate the higher electrophilic power of the structure.[39,40]

$$\mu = -\chi = -(E_{HOMO} + E_{LUMO})/2 \quad (4)$$

$$\eta = (E_{LUMO} - E_{HOMO})/2 \quad (5)$$

$$\omega = \mu^2/2\eta \quad (6)$$

The ionization energy (I) and electron affinity (A) can be expressed as $-E_{HOMO}$ and $-E_{LUMO}$, respectively. Chemical shielding (CS) calculations were performed using the gauge-including atomic orbital (GIAO) method.[41] The chemical shift isotropy (σ_{iso}) and anisotropy ($\Delta\sigma$) parameters were calculated applying principal components ($\sigma_{11} \leq \sigma_{22} \leq \sigma_{33}$) of the chemical shift tensor, as follows:

$$\sigma_{iso}\ (\text{ppm}) = (\sigma_{11} + \sigma_{22} + \sigma_{33})/3 \quad (7)$$

$$\Delta\sigma\ (\text{ppm}) = \sigma_{33} - (\sigma_{11} + \sigma_{22})/2 \quad (8)$$

The NBO and AIM analysis was carried out at the M06-2X/6-31G(d) level of theory.[38,42]

Results and discussion

Optimized geometry of the adsorbents

The fully optimized geometry, highest occupied molecular orbital (HOMO), lowest unoccupied molecular orbital (LUMO), and molecular electrostatic potential (MEP) maps of the adsorbent nanocages (C_{24}, $C_{18}B_3N_3$, and $C_{12}B_6N_6$) are shown in Fig. 1. The optimized structures of these nanocages are characterized by two hexagons joined by twelve pentagons with D6, C3, and C3 point groups for C_{24}, $C_{18}B_3N_3$, and $C_{12}B_6N_6$, respectively. The C–C bond length within the hexagons of C_{24} is about 1.42 Å; however, the value of the C–C bond length is in the

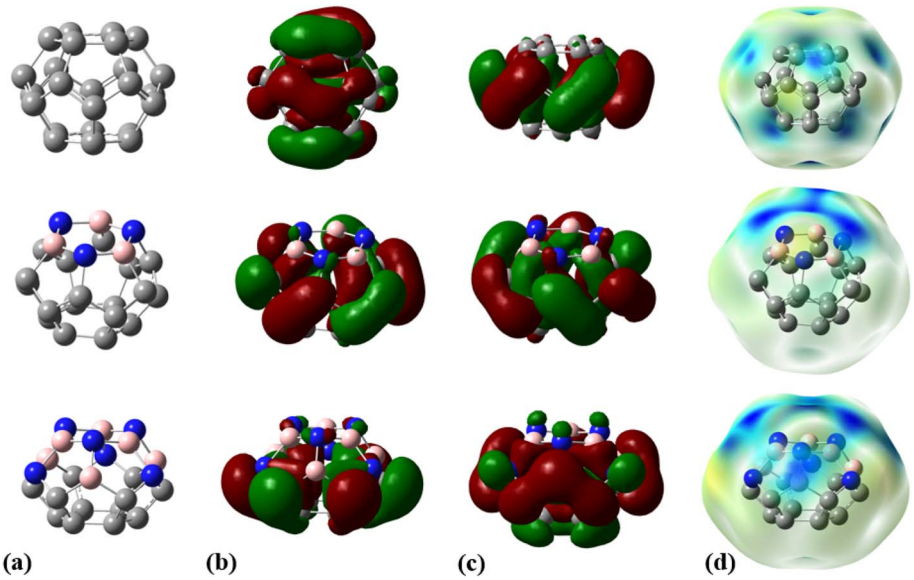

Fig. 1 (a) Optimized geometries, (b) HOMOs, (c) LUMOs, and (d) MEP plots for C_{24}, $C_{18}B_3N_3$, and $C_{12}B_6N_6$ nanocages at the M06-2X/6-31G(d,p) level of theory.

range of 1.36 Å to 1.53 Å in pentagons. The average value of the C–C bond length is calculated to be about 1.44 Å, which is in agreement with the reported values in the literature.[43,44] The $C_{18}B_3N_3$ is derived by substituting the carbon atoms of a hexagon of C_{24} with boron and nitrogen atoms as one in between. Thus, $C_{18}B_3N_3$ includes a B_3N_3 ring, six pentagons with C_3BN formula, six pentagons with C_5 formula, and a C_6 ring. The average length of C–C, B–C, N–C, and B–N bonds is about 1.47, 1.57, 1.46, and 1.48 Å, respectively. In the structure of $C_{12}B_6N_6$, five distinct types of rings are present: a B_3N_3 ring, six pentagons with B_2N_2C formula, three C_4N pentagons, three C_4B pentagons, and a C_6 ring. Here, the C–C, B–C, N–C, and B–N average bond lengths are about 1.47 Å, 1.54 Å, 1.41 Å, and 1.50 Å, respectively.

The molecular electrostatic potential (MEP) plot is a valuable tool for determining the electron density distribution over the atoms of a molecule and predicting its most reactive sites. It is widely known that the chemical and physical properties of a molecule are associated with its electrostatic potential. Therefore, the MEP plot can be utilized to characterize electrophilic and nucleophilic sites within an electrostatic interaction.[45] In a MEP contour, the surfaces are defined based on electron density and represented by an RGB color model, in which red regions are more negative than −0.010 a.u., yellow shows the regions with electron density between 0 and −0.010 a.u., green regions are between 0.010 and 0.0 a.u., and blue color represents regions more positive than 0.010 a.u. Fig. 2 reveals that O13, N8, and N10 atoms are the most negatively charged centers of the PA molecule. Additionally, the oxygen atom is more prone to contribute to the nucleophilic attack. The most positive atoms are C12 (0.68 $|e|$), H9 (0.45 $|e|$), H16 (0.43 $|e|$), H11 (0.41 $|e|$), and H15 (0.42 $|e|$), respectively, as shown by NBO analysis, which is in agreement with the MEP plot of the PA molecule.

The frequency calculations were performed at the M06-2X/6-31G(d,p) level of theory. The vibrational frequency modes of C_{24}, $C_{18}B_3N_3$, and $C_{12}B_6N_6$ appear in a positive range of 343–1630 cm^{-1}, 345–1603 cm^{-1}, and 282–1473 cm^{-1}, respectively, indicating that the optimized geometries are true local minima on the potential energy surface. Frontier molecular orbitals (HOMO and LUMO) of a molecule play a vital role in determining its reactivity. HOMO and LUMO energy levels are usually considered as the electron-donating and electron-accepting abilities of an organic molecule. A higher E_{HOMO} value indicates that the molecule can donate electrons, while a lower E_{LUMO} implies the molecule's willingness to accept electrons. Considering eqn (2), it can be concluded that molecules with a low HOMO–LUMO energy gap are more polarizable and have high chemical reactivity and low kinetic stability.[46] The HOMO levels of C_{24} are distributed over the C–C bonds throughout the nanocage except some C–C bonds in pentagons, whereas the LUMO levels are located on the C–C bonds of 5-membered rings. In the case of $C_{18}B_3N_3$ and $C_{12}B_6N_6$, the HOMO levels are mainly located on the N atoms and C–C bonds of pentagons, while the LUMO levels are situated on the B atoms and C–C bonds. The HOMO–LUMO energy gaps of C_{24}, $C_{18}B_3N_3$, and $C_{12}B_6N_6$ are about 3.92, 4.24, and 4.86 eV, respectively, indicating that these nanocages are semiconductors. In the following sections, we will discuss the role of frontier molecular orbitals in the electronic properties of molecules.

Adsorption of PA on the C_{24} nanocage

Aimed at identifying the most stable C_{24}-PA configuration, we considered all probable orientations of the PA molecule on the surface of C_{24} using the MEP plots of adsorbent and adsorbate molecules. All initial configurations were optimized employing the B3LYP/6-31G(d), CAM-B3LYP/6-31G(d,p) and M06-2X/6-31G(d,p) levels of theory. The adsorption energies (E_{ads}) for

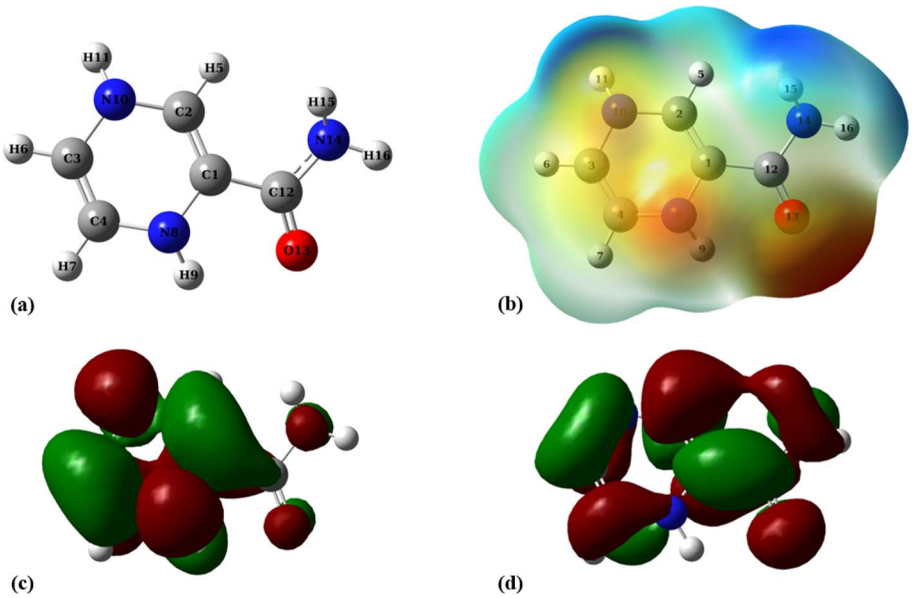

Fig. 2 (a) Optimized geometry, (b) MEP, (c) HOMO, and (d) LUMO profiles of PA at the M06-2X/6-31G(d,p) level of theory.

different configurations have been summarized in Table 1. More precisely it should be said that in the initial structures of C_{24}-PA, the drug molecule approached the 5- and 6-membered rings of C_{24} through (a) N8–H9, (b) N10–H11, (c) C12–O13, and (d) NH_2 group. The last configuration was the structure where PA is adsorbed in parallel on top of C_{24}. After careful optimization and performing vibrational frequency calculations, it was found that the drug molecule adopts a parallel orientation towards C_{24}. From Table 1, adsorption energies depend on both the method and basis set. Also, the energy difference between the configurations is significant in different methods. The amount of adsorption energy at the B3LYP/6-31G(d), CAM-B3LYP/6-31G(d,p), and M06-2X/6-31G(d,p) levels is −13.88 kJ mol^{-1}, −25.72 kJ mol^{-1}, and −125.58 kJ mol^{-1}, respectively. The minimum interaction distance between PA and C_{24} in the mentioned theoretical levels is 2.85 Å, 2.81 Å, and 2.82 Å, respectively (Fig. 3).

The values of enthalpy (ΔH) and Gibbs free energy changes (ΔG) of the C_{24}-PA complex are negative (with the exception of the B3LYP/6-31G(d) level), indicating that an exothermic and spontaneous reaction has occurred.

The changes in bond length and bond angles of the drug molecule, upon interaction with C_{24} at the M06-2X/6-31G(d,p) level of theory are illustrated in Tables 2 and S1,† respectively. The length of the C1–C2, C4–N8, C1–N8, N8–H9, and C12–O13 bonds increases while the length of other bonds decreases upon complexation. The results show that the interaction between the drug molecule and $C_{12}B_6N_6$ has no significant effect on the bond lengths of the PA molecule. The most obvious change in the bond angles of the PA molecule is related to the C12–N14–H16 angle, which ranges from 114.5° to 119.1°. Table 3 summarizes the quantum chemistry reactivity parameters of the nonionic surfactants, including E_{HOMO}, E_{LUMO}, and their associated energy gap (E_g), ionization potential (I), electron affinity (A),

Table 1 Adsorption energies (E_{ads}), enthalpy changes (ΔH), and Gibbs free energy changes (ΔG) calculated for C_{24}-PA, $C_{18}B_3N_3$-PA, and $C_{12}B_6N_6$-PA complexes at different levels of theory

Method	E_{ads} (kJ mol^{-1})	E_{ads}^{bsse} (kJ mol^{-1})	ΔH (kJ mol^{-1})	ΔG (kJ mol^{-1})
B3LYP/6-31G(d)				
C_{24}-PA	−13.88	−1.34	−9.86	27.48
$C_{18}B_3N_3$-PA	−25.72	−5.75	−22.16	21.98
$C_{12}B_6N_6$-PA	−125.58	−98.05	−120.99	−70.88
CAM-B3LYP/6-31G(d,p)				
C_{24}-PA	−14.81	−8.34	−9.57	−35.40
$C_{18}B_3N_3$-PA	−124.73	−97.78	−119.43	−68.50
$C_{12}B_6N_6$-PA	−138.55	−124.21	−309.76	−83.07
M06-2X/6-31G(d,p)				
C_{24}-PA	−45.95	−29.98	−40.08	−3.62
$C_{18}B_3N_3$-PA	−163.63	−56.62	−155.81	−95.25
$C_{12}B_6N_6$-PA	−156.48	−137.69	−150.71	−99.17

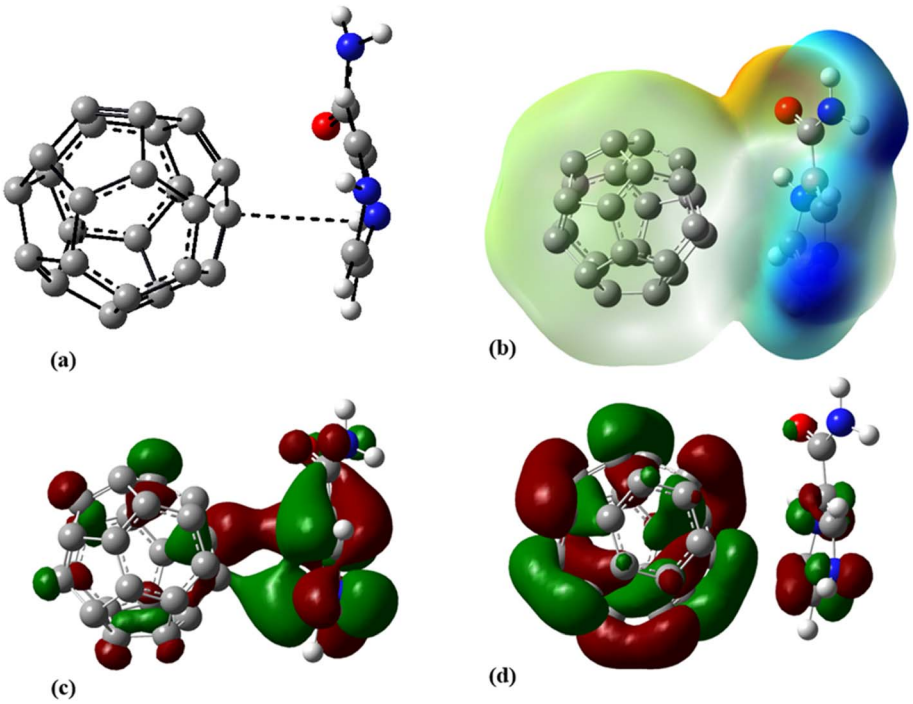

Fig. 3 (a) Optimized geometry, (b) MEP, (c) HOMO, and (d) LUMO profiles of C_{24}-PA at the M06-2X/6-31G(d,p) level of theory.

Table 2 Changes in the length of bonds of the PA molecule in interaction with C_{24} at the M06-2X/6-31G(d,p) level of theory

	Bond length (Å)		
Bond	After interaction	Before interaction	Δr
C1–C2	1.343	1.341	0.002
C3–C4	1.331	1.333	−0.002
C2–H5	1.083	1.085	−0.002
C3–H6	1.081	1.082	−0.001
C4–H7	1.082	1.083	−0.001
C4–N8	1.418	1.403	0.015
N8–H9	1.017	1.011	0.006
C1–N8	1.425	1.407	0.018
C2–N10	1.400	1.413	−0.013
C3–N10	1.423	1.434	−0.011
N10–H11	1.011	1.016	−0.005
C1–C12	1.481	1.486	−0.005
C12–O13	1.223	1.221	0.002
C12–N14	1.367	1.369	−0.002
N14–H15	1.009	1.009	0.000
N14–H16	1.007	1.007	0.000

electronegativity (χ), electronic chemical potential (μ), chemical hardness (η), electrophilicity index (ω), and dipole moments (in Debye). Frontier molecular orbital (FMO) analysis implies that the E_{HOMO} and E_{LUMO} of C_{24} become more stable by about 1.15 and 0.29 eV, respectively, upon complex formation (Fig. 4). Therefore, the E_g value decreases by 21.9%; thus, the electronic properties of C_{24} change considerably in the presence of PA molecules. The reduction of parameters ω, χ, A, and I is in agreement with the reduction of E_g. It is also observed that with the decrease of the E_g value, the softness and chemical hardness have increased and decreased, respectively, which indicates the tendency of the nanocarrier to interact with PA. The decrease in electrophilicity by 0.42 eV after interaction with the PA molecule confirms the charge transfer from the drug to the nanocarrier. The dipole moment of the C_{24}-PA complex is significantly higher than that of its components. Therefore, the solubility of the C_{24}-PA complex is expected to be higher than the solubility of C_{24} and PA.

The mechanism of action of a chemical sensor is directly related to the change in its resistance due to charge exchange with the chemical agent. It is known that the E_g is a dependable indicator to determine the sensitivity of a sensor towards a molecule. The electrical conductivity of a molecule decreases with increasing E_g.[47,48] The population of conduction electrons of a nanostructure increases significantly upon the decrease of E_g and *vice versa*. Changing the population of conducting electrons after the adsorption process causes the generation of an electrical signal.[49] The work function (Φ) is another electronic parameter that is affected by the adsorption process and is defined as the minimum amount of energy (*i.e.*, thermodynamic work) required to remove an electron from a solid to a point in the vacuum immediately outside the solid surface (*i.e.*, the Fermi level) and is defined as follows:

$$\Phi = V_{el(+\infty)} - E_F \quad (9)$$

where E_F is the energy of the Fermi level and $V_{el(+\infty)}$ is the electron electrostatic potential energy far from the solid surface. The value of $V_{el(+\infty)}$ is estimated to be zero, and therefore, we can write eqn (9) as $\Phi = -E_F$. The energy of the Fermi level is given as:

Table 3 Frontier molecular orbital energies (E_{HOMO} and E_{LUMO}) and their associated energy gaps (E_g) as well as CDFT parameters for the investigated structures at the M06-2X/6-31G(d,p) level of theory

Structure	E_{HOMO} (eV)	E_{LUMO} (eV)	E_g (eV)	E_F (eV)	I (eV)	A (eV)	χ (eV)	η (eV)	μ (eV)	S (1/eV)	ω (eV)	μ (Debye)
PA	−5.68	0.31	5.99	0.15	5.68	−0.31	2.69	3.00	−2.69	0.17	1.20	2.73
C_{24}	−6.92	−3.00	3.92	−1.50	6.92	3.00	4.96	1.96	−4.96	0.25	6.27	0.00
C_{24}-PA	−5.77	−2.70	3.06	−1.35	5.77	2.70	4.24	1.53	−4.24	0.33	5.86	3.79
$C_{18}B_3N_3$	−7.04	−2.80	4.24	−1.40	7.04	2.80	4.92	2.12	−4.92	0.24	5.70	1.10
$C_{18}B_3N_3$-PA	−5.84	−1.65	4.19	−0.83	5.84	1.65	3.75	2.10	−3.75	0.24	3.35	11.46
$C_{12}B_6N_6$	−7.14	−2.27	4.87	−1.14	7.14	2.27	4.70	2.43	−4.70	0.21	4.55	2.10
$C_{12}B_6N_6$-PA	−6.00	−1.38	4.62	−0.69	6.00	1.38	3.69	2.31	−3.69	0.22	2.95	14.48

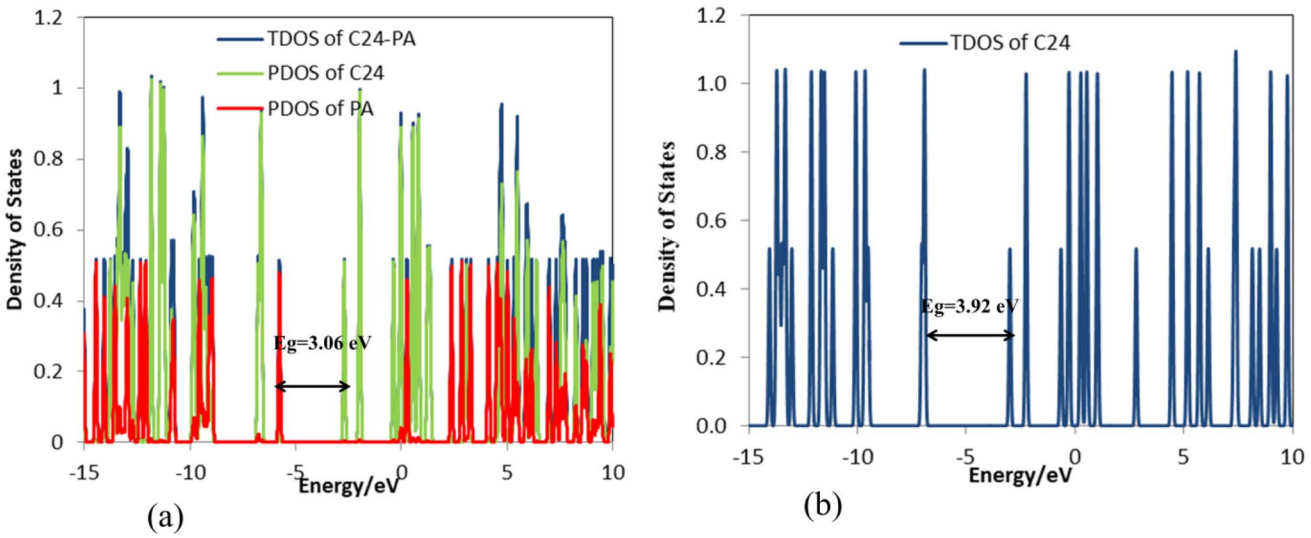

Fig. 4 DOS plots of (a) C_{24}-PA and (b) C_{24}.

$$E_F = E_{HOMO} + (E_{LUMO} - E_{HOMO})/2 \quad (10)$$

The Φ-type sensors apply a Kelvin oscillator instrument to calculate the values of Φ before and after adsorption.[32,50] In these sensors, the adsorption of a molecule changes the gate voltage and produces an electrical signal that leads to chemical agent detection.[51] The value of Φ is changed by about −0.147 eV going from C_{24} to C_{24}-PA; therefore, C_{24} can be used as a Φ-type sensor for PA detection.

To understand the donor–acceptor (bond–antibond) interactions between the drug molecule and the nanocages, NBO analysis has been performed at the M06-2X/6-31G(d,p) level of theory. In this analysis, all possible interactions between filled (donors) Lewis-type NBOs and empty (acceptors) non-Lewis NBOs are examined. Then, their energetic relevance is evaluated by second order perturbation theory. These interactions are called delocalization corrections to the zeroth-order natural Lewis structure because they result in a donation of electrons from the localized NBOs of the idealized Lewis structure into the empty non-Lewis orbitals. The stabilization energy ($E^{(2)}$) associated with delocalization $i \rightarrow j$ is defined as:

$$E^{(2)} = \Delta E_{ij} = q_i \frac{F(i-j)^2}{\varepsilon_j - \varepsilon_i} \quad (11)$$

where q_i is the donor orbital occupancy, ε_i and ε_j are diagonal elements (orbital energies), and $F(i,j)$ is the off-diagonal NBO Fock matrix element. This equation states a direct relationship between the off-diagonal NBO Fock matrix element and the orbital overlap. The greater values of $E^{(2)}$ indicate stronger interactions. The NBO analysis results showed that the highest values of stabilization energies $E^{(2)}$ of the C_{24} nanocarrier are: BD*(2) C12–C13 → BD*(2) C18–C19; $E^{(2)}$ = 30.29 kcal mol^{-1}, BD*(2) C10–C11 → BD*(2) C2–C16; $E^{(2)}$ = 30.36 kcal mol^{-1}, BD*(2) C21–C22 → BD*(2) C18–C19; $E^{(2)}$ = 22.63 kcal mol^{-1}, BD*(2) C9–C24 → BD*(2) C6–C7; $E^{(2)}$ = 30.47 kcal mol^{-1}, and BD*(2) C21–C22 → BD*(2) C15–C17; $E^{(2)}$ = 30.36 kcal mol^{-1}. Additionally, the most important stabilization energies related to the interaction of C_{24} and PA are BD (1) C3–C4 → RY*(3) C26; $E^{(2)}$ = 0.48 kcal mol^{-1} and BD(2) C3–C4 → BD*(2)C26–C27; $E^{(2)}$ = 3.19 kcal mol^{-1}. The changes in the atomic charges of the PA molecule due to the interaction with C_{24} are shown in Table S2† and confirm a charge transfer of 0.07 $|e|$ from the drug to the nanocarrier. A closer look into the atomic charges shows that the partial charge of C1, C2, C3, and N10 atoms has decreased by about 0.016, 0.018, 0.012, and 0.033 $|e|$ after the adsorption process. However, no noticeable change is observed in the charge of other atoms. The calculated partial atomic charges using the NBO technique are in good agreement with the MEP

plots. Comparing the MEP plots of C_{24} and PA molecules with that of the C_{24}-PA complex shows that the interaction between the drug molecule and the nanocarrier causes the transfer of electron density from PA to the nanocage. The contours in Fig. S1† show the atoms involved in electron resonance in C_{24}-PA, $C_{18}B_3N_3$-PA, and $C_{12}B_6N_6$-PA complexes. As seen, most of the atoms in the structure of the complexes contribute to the resonance interactions.

Adsorption of PA on the $C_{18}B_3N_3$ nanocage

To improve the interaction between the C_{24} and PA drug molecule, we adopted the doping technique so that six carbon atoms were replaced by three boron and three nitrogen atoms to form the $C_{18}B_3N_3$ nanocage. The most stable complex between $C_{18}B_3N_3$ and the PA drug molecule was obtained by adopting a method similar to that used for C_{24}-PA. The drug molecule approached the 5- and 6-membered rings of $C_{18}B_3N_3$, B, and N heteroatoms through (a) N8–H9, (b) N10–H11, (c) C12–O13, and (d) NH_2 group. Adsorption of PA on the surface of the $C_{18}B_3N_3$ nanocage is an exothermic process. The adsorption energies of PA on the $C_{18}B_3N_3$ at the mentioned levels of theory are reported in Table 1. The nearest interaction distance between PA and $C_{18}B_3N_3$ is 1.5 Å, in which the drug molecule has adopted a parallel orientation towards $C_{18}B_3N_3$ (Fig. 5). It seems that the weak π–π interactions are also effective in stabilizing the $C_{18}B_3N_3$ complex. The values of ΔH and ΔG of the $C_{18}B_3N_3$-PA complex at $T = 298$ K and $P = 1$ atm are shown in Table 1, which are more negative than the corresponding values of C_{24}-PA.

Table 4 Change in the length of bonds of the PA molecule upon interaction with $C_{18}B_3N_3$ PA at the M06-2X/6-31G(d,p) level of theory

	Bond length (Å)		
Bond	After interaction	Before interaction	Δr
C1–C2	1.352	1.341	0.012
C3–C4	1.331	1.333	−0.002
C2–H5	1.084	1.085	−0.001
C3–H6	1.080	1.082	−0.002
C4–H7	1.082	1.083	−0.001
C4–N8	1.423	1.403	0.02
N8–H9	1.019	1.011	0.008
C1–N8	1.427	1.407	0.020
C2–N10	1.375	1.413	−0.038
C3–N10	1.427	1.434	−0.0.007
N10–H11	1.011	1.016	−0.005
C1–C12	1.450	1.486	−0.036
C12–O13	1.284	1.221	0.063
C12–N14	1.324	1.369	−0.045
N14–H15	1.008	1.007	0.001
N14–H16	1.011	1.009	0.002

Tables 4 and S3† show the structural parameters (bond lengths and bond angles) of the drug molecule before and after interaction with the $C_{18}B_3N_3$ nanostructure. The interaction between the drug molecule and $C_{18}B_3N_3$ does not have a significant effect on the length of bond of the PA molecule and is similar to the structure of C_{24}PA. In any case, these changes are very small and can be ignored. The greatest decrease in the bond angle due to PA adsorption on the $C_{18}B_3N_3$ surface is related to the C4–N8–H9 angle, which decreased by 8.8°, while

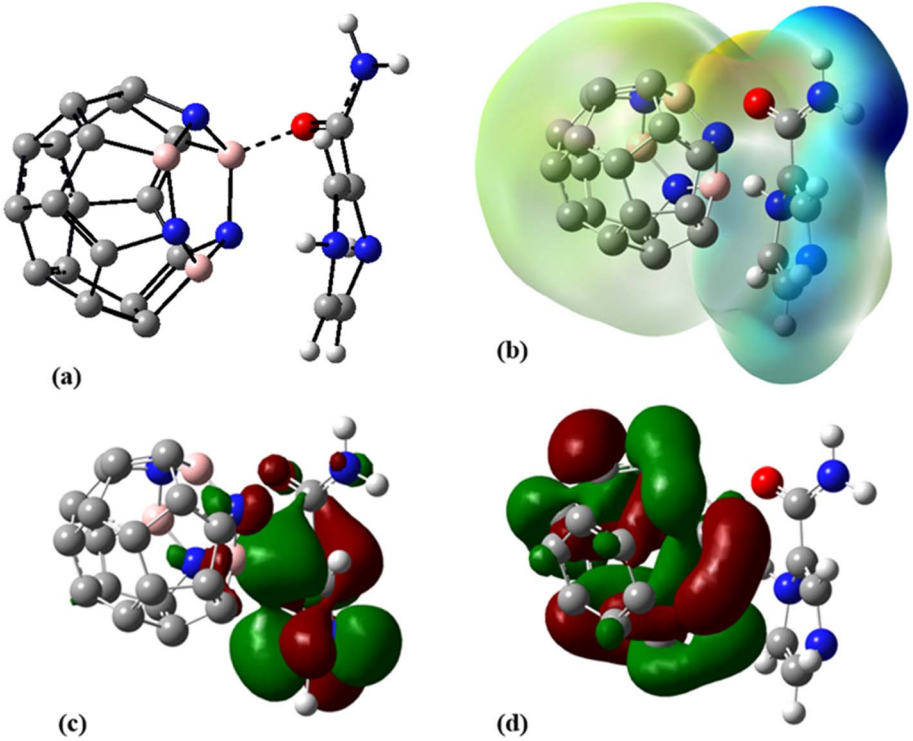

Fig. 5 (a) Optimized geometry, (b) MEP, (c) HOMO, and (d) LUMO profiles of $C_{18}B_3N_3$-PA at the M06-2X/6-31G(d,p) level of theory.

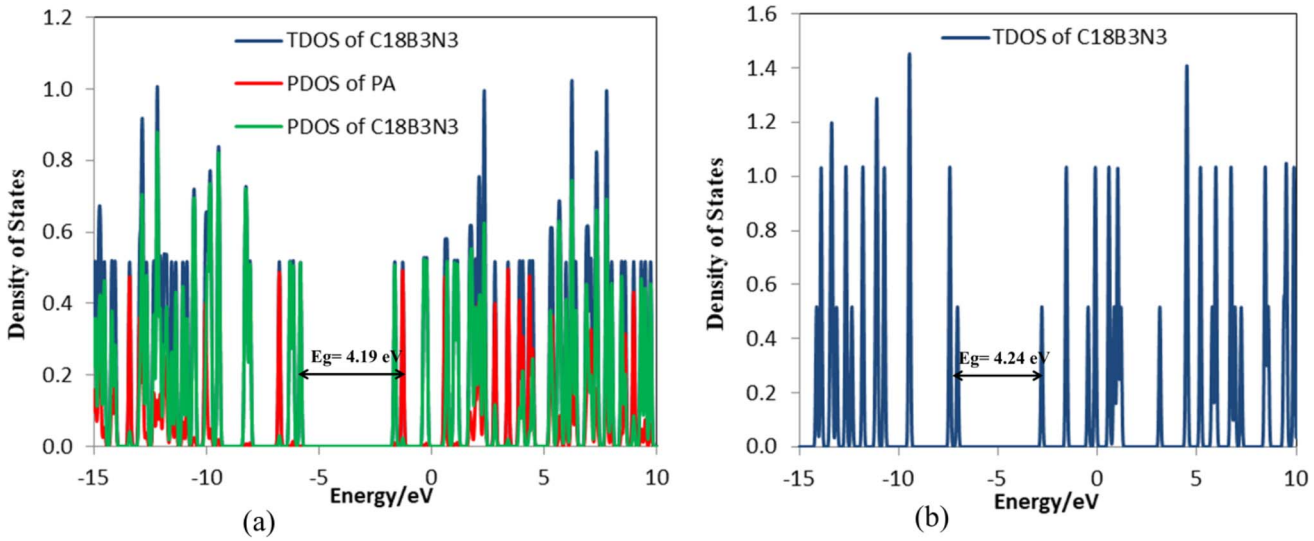

Fig. 6 DOS plots of (a) $C_{18}B_3N_3$-PA and (b) $C_{18}B_3N_3$.

C12–N14–H15 and C1–C12–N14 bond angles show increases of 3.8° and 2.6°, respectively. Frontier molecular orbital (FMO) analysis reveals that E_{HOMO} of $C_{18}B_3N_3$ changes from −7.04 eV to −5.84 eV after adsorption of PA; also, E_{LUMO} stabilizes by approximately 1.14 eV (Fig. 5). Therefore, the E_g value decreases by 1.2%; thus, the electronic properties of $C_{18}B_3N_3$ are sensitive to the presence of PA molecules. Here again the reductions in parameters ω, χ, A, and I are in agreement with the reduction in E_g (Fig. 6).

The decrease in electrophilicity upon adsorption of PA is calculated to be approximately 0.159 eV, showing that charge transfers from the drug molecule to $C_{18}B_3N_3$. Table S4† represents the partial atomic charges of the PA molecule before and after interaction with $C_{18}B_3N_3$. The charge of C1, C4, N8, and O13 atoms increased by approximately 0.048, 0.012, 0.001, and 0.022 $|e|$, respectively. The comparison of the total atomic charges of PA and $C_{18}B_3N_3$ shows that due to the formation of a complex between PA and $C_{18}B_3N_3$, 0.398 $|e|$ of charge is transferred from the drug to the nanocarrier.

The NBO analysis results showed that the highest values of stabilization energies $E^{(2)}$ of the $C_{18}B_3N_3$ nanocarrier are BD*(2) C33–C34 → BD*(2) C23–C24; $E^{(2)}$ = 49.82 kcal mol^{-1}, BD*(2) C29–C30 → BD*(2) C31–C32; $E^{(2)}$ = 50.27 kcal mol^{-1}, BD*(2) C27–C28 → BD*(2) C25–C26; $E^{(2)}$ = 49.69 kcal mol^{-1}, BD(2) C33–C34 → LP*(1) B21; $E^{(2)}$ = 45.12 kcal mol^{-1}, and BD(2) C25–C26 → LP*(1) B21; $E^{(2)}$ = 44.91 kcal mol^{-1}. The antibonding orbitals of boron atoms are the most important non-Lewis acceptors. The greatest values of stabilization energy in the $C_{18}B_3N_3$-PA complex are related to transitions within the $C_{18}B_3N_3$ molecule: BD*(2) C33–C34 → BD*(2) C23–C24; $E^{(2)}$ = 34.89 kcal mol^{-1}, BD*(2) C29–C30 → BD*(2) C31–C32; $E^{(2)}$ = 42.29 kcal mol^{-1}, BD*(2) C27–C28 → BD*(2) C25–C26; $E^{(2)}$ = 37.10 kcal mol^{-1}, and BD*(2) C37–C36 → BD*(2) C23–C24; $E^{(2)}$ = 57.13 kcal mol^{-1}. The most important stabilization energies related to the interaction between $C_{18}B_3N_3$ and PA are BD(2) C25–C26 → LP*(1) B21; $E^{(2)}$ = 46.33 kcal mol^{-1} and BD(1) C25–C26 → LP*(1) B21; $E^{(2)}$ = 3.43 kcal mol^{-1}, which indicates charge transfer from the drug molecule to $C_{18}B_3N_3$.

Adsorption of PA on the $C_{12}B_6N_6$ nanocage

In the next step, 12 carbon atoms of C_{24} were replaced by six boron atoms and six nitrogen atoms to obtain the $C_{12}B_6N_6$ structure. In the most stable $C_{12}B_6N_6$-PA complex, the oxygen atom of the drug molecule has established a bond with one of the boron atoms of the nanostructure with a length of 1.523 Å, which leads to an adsorption energy of −125.58 kJ mol^{-1}, −138.55 kJ mol^{-1}, and −156.48 kJ mol^{-1} at the B3LYP/6-31G(d), CAM-B3LYP/6-31G(d,p), and M06-2X/6-31G(d,p) levels of theory, respectively (Fig. 7 and Table 1).

Table 5 shows that despite the relatively strong interaction between the drug molecule and $C_{12}B_6N_6$, the geometrical parameters of PA did not change significantly. However, the bond length changes are more evident in the areas involved in the interaction with the nanostructure. For example, after forming the $C_{12}B_6N_6$-PA complex, the C–O bond length of PA has increased by approximately 0.057 Å. The process of bond length changes in $C_{12}B_6N_6$-PA is similar to that in the $C_{18}B_3N_3$-PA and C_{24}-PA complexes. Additionally, the lengths of C1–C12 and C1–N8 bonds increased, which can be attributed to resonance effects. The highest bond angle increase due to PA adsorption on the $C_{12}B_6N_6$ surface is related to C1–C12–N14, C2–N10–H11, and C12–N14–H16 angles, which increased by 4.7°, 2.5° and 2.4°, respectively. The C1–C12–O13 bond angle decreased from 120.1° to 115.4° (Table S5†).

According to Table 3, the E_g of $C_{12}B_6N_6$ has decreased by 0.24 eV after interaction with the drug molecule, which indicates the high reactivity of the nanocarrier (Fig. 8). The significant decrease of E_g shows that the electronic properties of $C_{12}B_6N_6$ are very sensitive to the presence of drug molecules in the environment, and therefore, $C_{12}B_6N_6$ can be used as a PA sensor. The reduction in parameters ω, χ, A, and I is in agreement with the reduction in E_g. It is also observed that with the

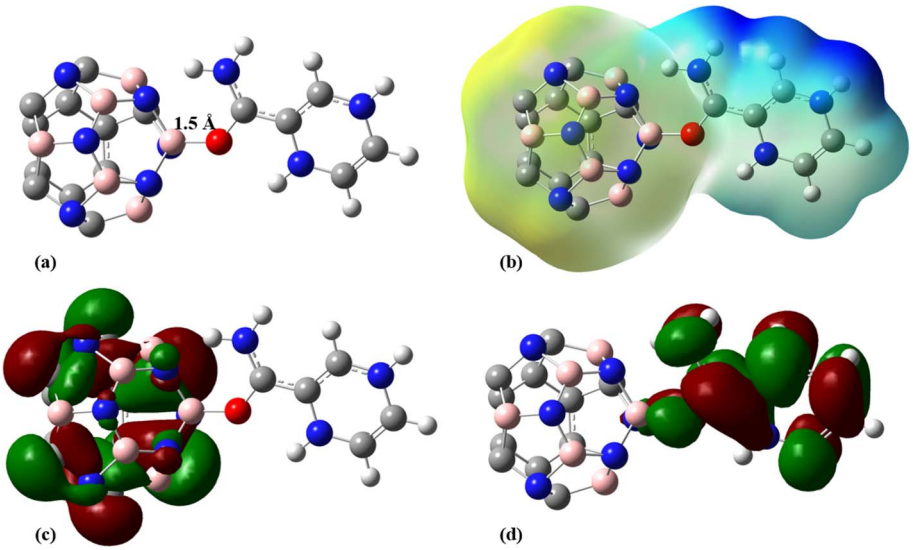

Fig. 7 (a) Optimized geometry, (b) MEP, (c) HOMO, and (d) LUMO profiles of $C_{12}B_6N_6$-PA at the M06-2X/6-31G(d,p) level pf theory.

Table 5 Change in the length of bonds of the PA molecule upon interaction with $C_{12}B_6N_6$ at the M06-2X/6-31G(d,p) level of theory

	Bond length (Å)		
Bond	After interaction	Before interaction	Δr
C1–C2	1.350	1.341	0.009
C3–C4	1.329	1.333	−0.004
C2–H5	1.084	1.085	−0.001
C3–H6	1.080	1.082	−0.002
C4–H7	1.081	1.083	−0.002
C4–N8	1.416	1.403	0.013
N8–H9	1.014	1.011	0.003
C1–N8	1.425	1.407	0.018
C2–N10	1.375	1.413	−0.038
C3–N10	1.433	1.434	−0.001
N10–H11	1.009	1.016	−0.007
C1–C12	1.450	1.486	−0.036
C12–O13	1.278	1.221	0.057
C12–N14	1.326	1.369	−0.043
N14–H15	1.006	1.007	−0.001
N14–H16	1.024	1.009	0.015

decrease in the E_g value, the softness and chemical hardness have increased and decreased, respectively, which indicates the tendency of the nanocarrier to interact with the PA molecule. A considerable decrease in the electrophilicity parameter by 1.60 eV confirms the charge transfer from the drug to the nanocarrier.

Table S6† shows that the partial charge of PA atoms is affected by the presence of the $C_{12}B_6N_6$ nanocarrier in the environment. Therefore, the charges of the C1, C3, N8, and O13 atoms increased by 0.029, 0.001, 0.009, and 0.020 $|e|$. On the other hand, the charges of the C2, N14 and N10 atoms have become more positive by 0.078, 0.067, and 0.053 $|e|$ respectively. Additionally, NBO calculations show that due to the formation of a complex between PA and $C_{12}B_6N_6$, a charge amount of 0.324 $|e|$ is transferred from the drug to the nanocarrier. The dipole moment is an important parameter for understanding the symmetry of the complex; the higher the dipole moment, the higher the interaction between the adsorbate and adsorbent molecules.[52] The significant increase in the dipole moment of $C_{12}B_6N_6$ indicates that the solubility of $C_{12}B_6N_6$-PA increases upon the adsorption process.

Examining the stabilization energies $E^{(2)}$ shows that the most important electron transfers of the drug molecule are: LP(1) N14 → BD*(2) C12–O13; $E^{(2)}$ = 56.14 kcal mol^{-1}, LP(1) N10 → BD*(2) C1–C2; $E^{(2)}$ = 34.28 kcal mol^{-1}, LP(1) N8 → BD*(2) C1–C2; $E^{(2)}$ = 33.13 kcal mol^{-1}, LP(2) O13 → BD*(1) C12–N14; $E^{(2)}$ = 29.41 kcal mol^{-1}, and BD(2) C1–C2 → BD*(2) C12–O13; $E^{(2)}$ = 19.41 kcal mol^{-1}. The most important donors are free electron pairs of nitrogen and oxygen that fill the C1–C2 and C12–O13 antibonding orbitals. Additionally, the greatest stabilization energy $E^{(2)}$ values of the nanocarrier are: LP(1) N25 → LP*(1) B17; $E^{(2)}$ = 24.73 kcal mol^{-1}, LP(1) N29 → LP*(1) B19; $E^{(2)}$ = 24.75 kcal mol^{-1}, BD(2) N17–B19 → LP*(1) B19; $E^{(2)}$ = 62.33 kcal mol^{-1}, BD(2) N17–B19 → LP*(1) B121; $E^{(2)}$ = 63.09 kcal mol^{-1}, and BD(2) N33–B21 → LP*(1) B19; $E^{(2)}$ = 62.86 kcal mol^{-1}. As seen, non-Lewis acceptors are antibonding orbitals of boron atoms. Regarding the donor–acceptor transitions in the $C_{12}B_6N_6$-PA complex, it should be said that the largest amounts of stabilization energy are related to transitions within the $C_{12}B_6N_6$ molecule which are: BD*(2) C24–N25 → LP*(1) B23; $E^{(2)}$ = 99.29 kcal mol^{-1}, LP(1) C2 → LP*(1) C4; $E^{(2)}$ = 90.21 kcal mol^{-1}, LP(1) C26 → BD*(2) C24–N25; $E^{(2)}$ = 74.59 kcal mol^{-1}, BD(2) N27–B18 → LP*(1) B17; $E^{(2)}$ = 70.14 kcal mol^{-1}, and BD*(2) C12–N14 → BD*(2) C1–C2; $E^{(2)}$ = 69.22 kcal mol^{-1}. The most important stabilization energies related to the interaction between $C_{12}B_6N_6$ and PA are: BD(2) B17–N18 → BD*(1) B17–O13; $E^{(2)}$ = 13.34 kcal mol^{-1}, LP(2) O13 → BD*(1) B17–N25; $E^{(2)}$ = 6.22 kcal mol^{-1}, and BD(2) C12–N14 → BD*(1) B17–O; $E^{(2)}$ = 1.35 kcal mol^{-1}, which is in agreement with the increase of the C12–O13 bond and also bond formation between the PA oxygen and the boron atom of

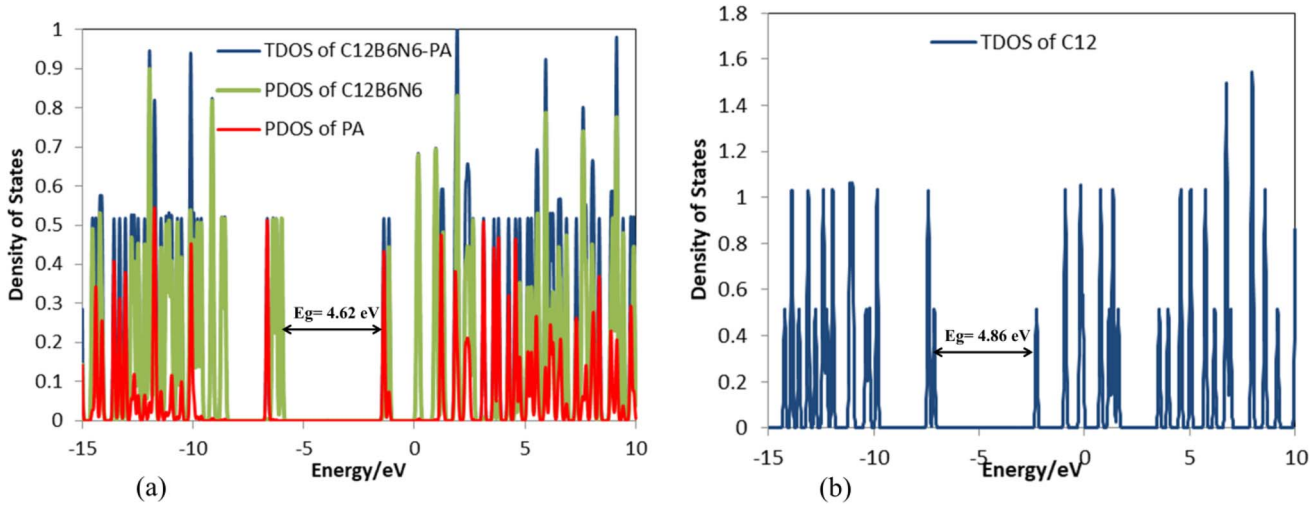

Fig. 8 DOS plots of (a) $C_{12}B_6N_6$-PA and (b) $C_{12}B_6N_6$.

$C_{12}B_6N_6$. As can be seen, the replacement of carbon atoms with boron and nitrogen atoms increased the stabilization energies.

Atoms in molecule analysis

Bader's quantum theory of atoms in molecules (QTAIM)[53] was utilized to explore electron density and bonding characteristics of the investigated systems. This theory states that upon chemical bond formation between two atoms a bond critical point (BCP) appears between them. The characteristics of BCPs are of great relevance in determining the electron density (ρ_C) and its corresponding Laplacian ($\nabla^2\rho_C$), and therefore, designating the nature of interactions at a molecular level. $\nabla^2\rho_C$ is the second derivative of a scalar function and provides information about the tendency of electron density to concentrate or deplete. The total electronic energy density at the BCP (H_C) elucidates the energetic properties of BCPs and it is the sum of the local kinetic energy density (G_C) and local potential energy density (V_C) at the BCP.

$$H_C = G_C + V_C \quad (12)$$

On the other hand, the virial theorem states a relation between the Laplacian of the electron density at BCP and its other characteristics.

$$(1/4)\nabla^2\rho_C = 2G_C + V_C \quad (13)$$

A negative value of the Laplacian indicates the concentration of the electron density among the nuclei of interacting atoms, and one may assume a shared interaction such as covalent bonds and lone pairs. A positive Laplacian electron density value at corresponding BCP shows the depletion of electron density as in ionic, van der Waals, and hydrogen bond interactions. Fig. 9 illustrates the molecular graph of C_{24}-PA, $C_{18}B_3N_3$-PA, and $C_{12}B_6N_6$-PA complexes obtained from AIM calculations. The graphs were obtained at the M06-2X/6-31G(d,p) level of theory. Large circles correspond to attractors and small red and yellow circles are bond and ring critical points, respectively. However, sometimes $\nabla^2\rho_C > 0$ but the total electronic energy density, H_C, is negative and such a situation is attributed to the partially covalent interaction. Fig. 9 shows that the adsorption of the PA molecule on the surface of the C_{24} nanocage led to the appearance of two critical points between the drug and the nanostructure. The electron density properties calculated for the C_{24}-PA complex reveal that for the $O13_{PA}\cdots$ C19 interaction $\nabla^2\rho_C > 0$ and $H_C > 0$; hence, this interaction belongs to the category of electrostatic interactions. The $C4_{PA}\cdots$ C20 interaction has more electron density (0.006 a.u.), and the

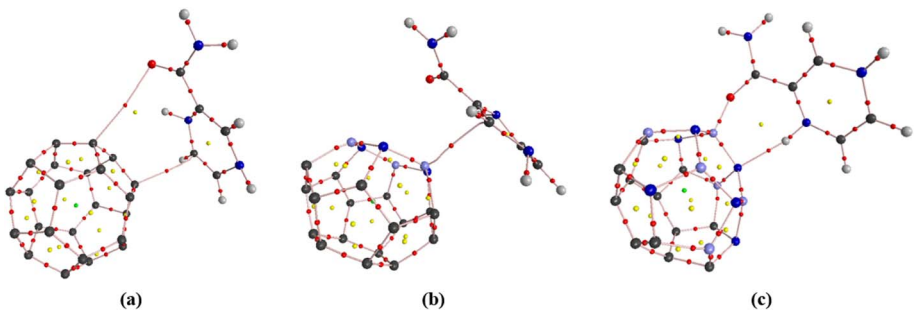

Fig. 9 Molecular graphs for C_{24}-PA, $C_{18}B_3N_3$-PA, and $C_{12}B_6N_6$-PA complexes at the M06-2X/6-31G(d,p) level of theory (large circles correspond to attractors, while small red and yellow circles are bond and ring critical points, respectively).

Table 6 Topological parameters (all in atomic units) for the optimized structures analyzed here at the M06-2X/6-31G(d,p) level of theory

Complex	Interaction site	ρ_C	$\nabla^2\rho_C$	G_C	V_C	H_C	Type of interaction
C_{24}-PA	O13(PA)···C19	0.010	0.031	0.007	−0.006	0.001	Electrostatic
	C4(PA)···C20	0.006	0.019	0.004	−0.003	0.001	
$C_{18}B_3N_3$-PA	O(PA)···B17	0.117	0.512	0.194	−0.259	−0.065	Partly covalent
$C_{12}B_6N_6$-PA	O13(PA)···B17	0.126	−0.138	0.209	−0.280	−0.071	Covalent
	H(PA)···N18	0.033	0.089	0.023	−0.024	−0.001	Partly covalent

values of $\nabla^2\rho_C$ (0.019 a.u.) and H_C (0.001 a.u.) are positive. Therefore, this bond is also the result of an electrostatic interaction (Table 6).

AIM calculations showed that only one critical point has appeared between O13 of the PA molecule and B17 of the $C_{18}B_3N_3$ nanostructure, for which the values of ρ_C, $\nabla^2\rho_C$ and H_C are 0.117, 0.512, and −0.065 a.u. respectively. Therefore, the O_{PA}···B17 interaction is partially covalent. The electron density properties calculated for the $C_{12}B_6N_6$-PA complex show that the $O13_{PA}$···B17 bond possesses a significant charge density (0.126 a.u.). Moreover, the values of $\nabla^2\rho_C$ (−0.138 a.u.) and H_C (−0.071 a.u.) are negative. Therefore, as we mentioned before, the $O13_{PA}$···B17 bond is a covalent interaction. AIM calculations show that the H_{PA}···N18 interaction has lower values of ρ_C and $\nabla^2\rho_C > 0$; however, this interaction is categorized as a partly covalent interaction because $\nabla^2\rho_C > 0$ and $H_C < 0$.

NMR and IR spectra

The changes in charge density around the nuclei involved in the adsorption process can be very efficient in verifying the nature of host–guest interactions because the magnitude of these variations reveals the contribution of each nucleus to the interaction.[54] Therefore, we performed NMR chemical shift calculations using the GIAO method to investigate the nature of interactions involved in the adsorption of PA on the surface of C_{24}, $C_{18}B_3N_3$, and $C_{12}B_6N_6$. The chemical shift (CS) principal components (σ_{ii}), CS isotropy (σ_{iso}), and CS anisotropy values of ^{13}C, ^{15}N, ^{17}O, and ^{1}H for the surfactant molecules calculated at the M06-2X/6-31G(d,p) level of theory are shown in Tables S7 to S13.† The isotropy (σ_{iso}) parameter shows the average value of the CS tensor, while the anisotropy ($\Delta\sigma$) parameter specifies the orientations of the CS tensor at the atomic site. The calculated chemical shift tensors for ^{13}C, ^{15}N, ^{17}O, and ^{1}H nuclei are sensitive to complex formation at the active site. The values of σ_{iso} and $\Delta\sigma$ parameters of the C12, O13, and N14 atoms of the drug molecule increase significantly due to the adsorption on $C_{12}B_6N_6$. After complex formation, the values of σ_{iso} and $\Delta\sigma$ of the N8 and N10 atoms in the PA molecule decrease and increase, respectively. The value of σ_{iso} for C1 to C4 atoms in the drug molecule increases, while the $\Delta\sigma$ value for these atoms decreases. The changes in the σ_{iso} and $\Delta\sigma$ values of the PA atoms in $C_{18}B_3N_3$-PA and C_{24}-PA complexes also follow the same trend. The values of σ_{iso} and $\Delta\sigma$ parameters of the C10, C11, C12, B13, B14, and B15 atoms of the $C_{12}B_6N_6$ nanocage increase due to complex formation, while the values of σ_{iso} and $\Delta\sigma$ of the C1, C5, C8, N18, B19, B20, N22, N23, and N24 atoms have decreased. In general, the results obtained from NMR spectra are in agreement with the previous results. Fig. S2 to S7† show the IR spectra of the compounds investigated in this study. Fig. S6† shows that a new peak appears in the region of 3300 cm^{-1} after $C_{12}B_6N_6$-PA complex formation, which indicates the interaction between the functional groups of the host and guest molecules. Although the interaction of the drug molecule with $C_{18}B_3N_3$ and C_{24} nanocarriers also leads to changes in the IR spectrum of the nanocages, due to the orientation of the interacting molecules, the intensity and the location of the peaks are different.

UV-Vis spectra

The interaction between light and matter has always been of interest and is used to investigate the electronic properties of molecules precisely. The UV-Vis spectrum of the PA molecule (Fig. S9†) shows that the highest peak corresponds to the wavelength of 228 nm with $f = 0.099$. The higher the value of f, the higher the transition peak. The highest peak for the $C_{12}B_6N_6$ molecule appears at 327 nm with $f = 0.002$ and for $C_{12}B_6N_6$-PA at 496 nm with $f = 0.069$. In general, as shown in Tables S15–S20 and Fig. S9–S14,† adsorption of PA on the surface of nanocarriers, the wavelengths of the C_{24}, $C_{18}B_3N_3$, and $C_{12}B_6N_6$, and thus, the highest peaks are shifted to higher values. Therefore, a redshift occurs after the adsorption process.

Conclusions

In this study, we investigated the potential of the pristine C_{24} nanocage and its doped boron nitride analogs ($C_{18}B_3N_3$ and $C_{12}B_6N_6$) as carriers for the pyrazinamide (PA) drug using density functional theory (DFT). All calculations including geometry optimization, vibrational frequencies, QTAIM, NBO, NMR, and IR were carried out using the B3LYP/6-31G(d), CAM-B3LYP/6-31G(d,p) and M06-2X/6-31G(d,p) levels of theory. To calculation of the dispersion energy, the modified CAM-B3LYP and M06-2X methods were used. The results show that the adsorption energies calculated by B3LYP, CAM-B3LYP, and M06-2X methods are different. The M06-2X values are greater than those calculated by B3LYP and CAM-B3LYP methods. The adsorption energy (E_{ads}), enthalpy (ΔH), and Gibbs free energy (ΔG) of C_{24}-PA, $C_{18}B_3N_3$-PA, and $C_{12}B_6N_6$-PA complexes were calculated using the B3LYP/6-31G(d), CAM-B3LYP/6-31G(d,p) and M06-2X/6-31G(d,p) levels of theory. The results show that the interaction of the drug with the nanocages is exothermic and a spontaneous reaction has occurred at all theoretical levels (with the exception of the B3LYP/6-31G(d) level for C_{24}-PA and $C_{18}B_3N_3$). The results show that doping has increased the

conductivity of nanocages. On the other hand, the interaction of PA with nanocages leads to a reduction in the energy gap of complexes. The E_g values of C_{24}, $C_{18}B_3N_3$, and $C_{12}B_6N_6$ at the M06-2X/6-31G(d,p) level decrease by approximately 21%, 1.2%, and 5%, respectively, upon complexation. Furthermore, the decrease of E_g in complexes suggests that nanocages can be utilized for sensing PA molecules. Despite the relatively strong interactions between the drug molecule and nanocages, the geometrical parameters of PA did not change significantly. The changes in the atomic charges of the PA molecule due to the interaction with C_{24}, $C_{18}B_3N_3$, and $C_{12}B_6N_6$ confirm a charge transfer of 0.07, 0.327, and 0.398 $|e|$ from the drug to the nanocage, respectively. Based on the NBO results, the replacement of carbon atoms with boron and nitrogen atoms increased the stabilization energies ($E^{(2)}$). AIM calculations revealed that the observed interactions between the nanocage and PA drug in $C_{12}B_6N_6$-PA and $C_{18}B_3N_3$-PA nanocages are stronger than those with the C_{24}-PA nanocage. The results show that all three types of nanocages can be used as drug delivery systems for PA molecules.

Ethics approval and consent to participate

This study did not involve human subjects, animal experimentation, or other activities necessitating ethical review.

Consent for publication

The authors of this manuscript confirm that all authors have reviewed and approved the final version of the manuscript for submission to the journal of *Nanoscale Advances*.

Data availability

The datasets generated during the current study are available upon request from the corresponding author. Additionally, some of the data and materials supporting this article have been included in the main text and ESI.†

Author contributions

F. Naderi: conceived and designed the study, reviewing, editing of the manuscript, conceptualization, supervision; A. Moumivand: writing, software; O. Moradi: validation, visualization, methodology; B. Makiabadi: editing of the manuscript.

Conflicts of interest

All authors declare that they have no competing interests.

Acknowledgements

No funding was received to assist with the preparation of this manuscript.

References

1 V. Kumar, A. K. Abbas, N. Fausto and R. N. Mitchell, Cervical cancer, in *Robbins Basic Pathology*, Saunders Elsevier, Philadelphia, 8th edn, 2007.
2 C. A. Whittle and C. G. Extavour, *Genome Biol. Evol.*, 2016, **8**, 2722–2736.
3 S. K. Sharma and A. Mohan, *Chest*, 2006, **130**, 261–272.
4 M. J. Reid, N. Arinaminpathy, A. Bloom, B. R. Bloom, C. Boehme, R. Chaisson, D. P. Chin, G. Churchyard, H. Cox and L. Ditiu, *The Lancet*, 2019, **393**, 1331–1384.
5 J. L. Khawbung, D. Nath and S. Chakraborty, *Comp. Immunol., Microbiol. Infect. Dis.*, 2021, **74**, 101574.
6 M. Najafimosleh, K. Ghazi-Saiedi, P. Farnia, F. Mohammadi and A. Velayati, *J. Clin. Microbiol.*, 2008, **11**, 14–21.
7 R. Esfandiarpour, F. Badalkhani-Khamseh and N. L. Hadipour, *Colloids Surf., B*, 2022, **215**, 112513.
8 S. Bazyari-Delavar, F. Badalkhani-Khamseh, A. Ebrahim-Habibi and N. L. Hadipour, *J. Nanopart. Res.*, 2021, **23**, 1–12.
9 F. Badalkhani-Khamseh, A. Ebrahim-Habibi, N. L. Hadipour and M. Behmanesh, *Chem. Eng. Sci.*, 2023, **267**, 118283.
10 M. Yahyavi, F. Badalkhani-Khamseh and N. L. Hadipour, *J. Mol. Liq.*, 2023, **377**, 121393.
11 U. Sahebi, H. Gholami, B. Ghalandari, F. Badalkhani-khamseh, A. Nikzamir and A. Divsalar, *J. Mol. Liq.*, 2021, **344**, 117758.
12 M. N Kumar, *J. Pharm. Pharm. Sci.*, 2000, **3**, 234–258.
13 W. Gao, G. Ye, X. Duan, X. Yang and V. C. Yang, *Int. J. Nanomed.*, 2017, **12**, 1047–1064.
14 M. A. A. Ibrahim, A.-s. S. M. Rady, A. M. A. Mandarawe, L. A. Mohamed, A. M. Shawky, T. H. A. Hasanin, P. A. Sidhom, M. E. S. Soliman and N. A. M. Moussa, *Pharmaceuticals*, 2022, **15**, 1181.
15 M. Zarghami Dehaghani, B. Bagheri, F. Yousefi, A. A Nasiriasayesh, A. H. Mashhadzadeh, P. Zarrintaj, N. Rabiee, M. Bagherzadeh, V. Fierro, A. Celzard, M. R. Saeb and E. Mostafavi, *Int. J. Nanomed.*, 2021, **16**, 1837–1847.
16 F. Naderi, *Russ. J. Phys. Chem. A*, 2016, **90**, 1385–1390.
17 M. Ashiq, M. N. Zahid, Y. Malik, A. A. Alghamdi, S. A. M. Abdelmohsen and J. Iqbal, *BioNanoSci*, 2024, 1–22.
18 F. B. Balıbey, F. Bahadori, G. E. Kizilcay, A. Tekin, E. Kanimdan and A. Kocyigit, *Pharm. Dev. Technol.*, 2023, **28**, 843–855.
19 M. Anafcheh, F. Naderi, Z. Khodadadi, F. Ektefa and R. Ghafouri, *Silicon*, 2019, **11**, 323.
20 F. Naderi and V. Veryazov, *J. Chem. Chem. Eng.*, 2017, **11**, 30–36.
21 J. Singh, P. Nayak, G. Singh, M. Khandai, R. R. Sarangi and M. K. Kar, *C-J. Carbon Res.*, 2023, **9**, 1–28.
22 J. M. Ashcroft, D. A. Tsyboulski, K. B. Hartman, T. Y. Zakharian, J. W. Marks, R. B. Weisman, M. G. Rosenblum and L. J. Wilson, *Chem. Commun.*, 2006, **28**, 3004–3006.
23 R. P. Singh and P. Ramarao, *Toxicol. Sci.*, 2013, **136**, 131–143.

24 M. Anafcheh, R. Ghafouri and F. Naderi, *Phys. E*, 2012, **44**, 1992–1998.
25 G. I. Giannopoulos, *Nanomater.*, 2022, **12**, 2711.
26 S. M. Sharker, *Int. J. Nanomed.*, 2019, **14**, 9983–9993.
27 Z. Edis, J. Wang, M. K. Waqas, M. Ijaz and M. Ijaz, *Int. J. Nanomed.*, 2021, **16**, 1313–1330, DOI: 10.2147/IJN.S289443.
28 H. Xu, X. Tu, G. Fan, Q. Wang, X. Wang and X. Chu, *J. Mol. Liq.*, 2020, **318**, 114315.
29 S. Bibi, S. Ur-rehman, L. Khalid, I. A. Bhatti, H. N. Bhatti, J. Iqbal, F. Q. Bai and H. X. Zhang, *RSC Adv.*, 2022, **12**, 2873–2887.
30 T. M. Joseph, D. K. Mahapatra, A. Esmaeili, L. Piszczyk, M. S. Hasanin, M. Kattali, J. Haponiuk and S. Thomas, *Nanomater.*, 2023, **13**, 574.
31 M. J. Frisch, G. W. Trucks, H. B. Schlegel, G. E. Scuseria, M. A. Robb, J. R. Cheeseman, G. Scalmani, V. Barone, G. A. Petersson, H. Nakatsuji, X. Li, M. Caricato, A. Marenich, J. Bloino, B. G. Janesko, R. Gomperts, B. Mennucci, H. P. Hratchian, J. V. Ortiz, A. F. Izmaylov, J. L. Sonnenberg, D. Williams-Young, F. Ding, F. Lipparini, F. Egidi, J. Goings, B. Peng, A. Petrone, T. Henderson, D. Ranasinghe, V. G. Zakrzewski, J. Gao, N. Rega, G. Zheng, W. Liang, M. Hada, M. Ehara, K. Toyota, R. Fukuda, J. Hasegawa, M. Ishida, T. Nakajima, Y. Honda, O. Kitao, H. Nakai, T. Vreven, K. Throssell, J. A. Montgomery Jr, J. E. Peralta, F. Ogliaro, M. Bearpark, J. J. Heyd, E. Brothers, K. N. Kudin, V. N. Staroverov, T. Keith, R. Kobayashi, J. Normand, K. Raghavachari, A. Rendell, J. C. Burant, S. S. Iyengar, J. Tomasi, M. Cossi, J. M. Millam, M. Klene, C. Adamo, R. Cammi, J. W. Ochterski, R. L. Martin, K. Morokuma, O. Farkas, J. B. Foresman and D. J. Fox, *Gaussian 09, Revision A.02*, Gaussian, Inc., Wallingford CT, 2016.
32 S. Bazyari-Delavar, F. Badalkhani-Khamseh, A. Ebrahim-Habibi and N. L. Hadipour, *Comput. Theor. Chem.*, 2020, **1189**, 112983.
33 K. Gholivand, L. Sarmadi-Babaee, M. Faraghi, F. Badalkhani-Khamseh and N. Fallah, *Chem. Phys. Impact*, 2022, **5**, 100099.
34 M. M. Francl, W. J. Pietro, W. Hehre, J. S. Binkley, M. S. Gordon, D. J. DeFrees and J. A. Pople, *J. Chem. Phys.*, 1982, **77**, 3654.
35 Y. Zhao and D. G. Truhlar, *Theor. Chem. Acc.*, 2006, **120**, 215–241.
36 J. S. Wright, C. Rowley and L. Chepelev, *Mol. Phys.*, 2005, **103**, 815–823.
37 T. Yanai, D. P. Tew and N. C. Handy, *Chem. Phys. Lett.*, 2004, **393**, 51–57.
38 E. D. Glendening, A. E. Reed, J. E. Carpenter and F. Weinhold, *NBO, Version 3.1*, Gaussian Inc., Pittsburgh, PA, 1992.
39 N. M. O'boyle, A. L. Tenderholt and K. M. Langner, *J. Comput. Chem.*, 2008, **29**, 839–845.
40 K. Gholivand, M. Faraghi, M. Mirzaei-Saatlo, F. Badalkhani-Khamseh, G. Salimi and A. Barzegari, *J. Mol. Struct.*, 2023, **1274**, 134505.
41 K. Wolinski, J. F. Hinton and P. Pulay, *J. Am. Chem. Soc.*, 1990, **112**, 8251–8260.
42 F. Biegler-König and J. Schönbohm, *J. Comput. Chem.*, 2002, **23**, 1489–1494.
43 Y. Chang, J. Zhang, H. Sun, B. Hong, Z. An and R. Wang, *Int. J. Quantum Chem.*, 2005, **105**, 142–147.
44 M. R. Hossain, M. M. Hasan, S. U. D. Shamim, T. Ferdous, M. A. Hossain and F. Ahmed, *Comput. Theor. Chem.*, 2021, **1197**, 113156.
45 R. Esfandiarpour, M. R. Hosseini, N. L. Hadipour and A. Bahrami, *J. Mol. Model.*, 2019, **25**, 163.
46 M. Salehpour, Z. Saadati and L. Asadi, *Comput. Theor. Chem.*, 2022, **1209**, 113573.
47 J. Beheshtian, M. Noei, H. Soleymanabadi and A. A. Peyghan, *Thin Solid Films*, 2013, **534**, 650–654.
48 E. Cagatay, P. Köhler, P. Lugli and A. Abdellah, *IEEE Sens. J.*, 2015, **15**, 3225–3233.
49 J. Blakemore, *Solid State Physics*, ed. 2nd ed., WB Saunders Company, 1974.
50 I. Baikie, S. Mackenzie, P. Estrup and J. Meyer, *Rev. Sci. Instrum.*, 1991, **62**, 1326–1332.
51 G. Korotcenkov, *Sensing Layers in Work-function-type Gas Sensors, Handbook of Gas Sensor Materials*, Springer, 2013.
52 A. S. Rad, P. Valipour, A. Gholizade and S. E. Mousavinezhad, *Chem. Phys. Lett.*, 2015, **639**, 29–35.
53 R. F. Bader, *Acc. Chem. Res.*, 1985, **18**, 9–15.
54 F. Badalkhani-Khamseh, A. Bahrami, A. Ebrahim-Habibi and N. L. Hadipour, *Chem. Phys. Lett.*, 2017, **684**, 103–112.